Role of Anisotropy, Frequency, and Interactions in Magnetic Hyperthermia Applications: Noninteracting Nanoparticles and Linear Chain Arrangements

Daniela Paola Valdés[1,2] Enio Lima, Jr.,[1] Roberto Daniel Zysler[1,2] Gerardo Fabián Goya[3] and Emilio De Biasi[1,2,*]

[1]*Instituto de Nanociencia y Nanotecnología, CNEA-CONICET, San Carlos de Bariloche, Río Negro R8402AGP, Argentina*
[2]*Instituto Balseiro, Universidad Nacional de Cuyo, San Carlos de Bariloche, Río Negro, Río Negro, Argentina*
[3]*Departamento de Física de la Materia Condensada, Instituto de Nanociencia y Materiales de Aragón (INMA), Universidad de Zaragoza, Zaragoza 50018, Spain*

Efforts by numerous research groups have provided a deeper insight into the physical mechanisms behind the power absorption of single-domain magnetic nanoparticles in magnetic-fluid-hyperthermia applications and theoretical models now account for the main experimental observations. However, the role of all parameters relevant to the magnetic relaxation remains a matter of debate. Here, we employ a nonlinear model for the magnetic relaxation of single-domain magnetic nanoparticles with uniaxial effective anisotropy and evaluate the influence of particle-intrinsic parameters as well as experimental conditions on the power absorption of both noninteracting and interacting systems (linear arrangements). These effects are assessed through the enclosed hysteresis area of the magnetization loops as a function of relative anisotropy h_K (the anisotropy field with respect to the amplitude of the ac field), i.e., the "area curve" of the system. These curves can be divided into four regions with distinct magnetic responses and boundaries that depend on the particle size, frequency of the applied field and interactions. Interactions change the effective anisotropy of the system and shift the area curve towards lower h_K values. For the low relative anisotropy range, dipolar interactions increase the area of the hysteresis loops [thus, the specific power absorption (SPA)], while they are detrimental or produce nonsignificant effects for the range of high relative anisotropy. Our study resolves seemingly contradictory results of interaction effects in linear arrangements recently reported in the literature. Simulations of randomly oriented particles and chains were contrasted with the oriented cases. An analytical approach and the thermal interpretation of its validity range are discussed, both aimed at the design of nanoparticles and the choice of the experimental conditions for optimal heating. We find that systems with low-thermal-fluctuation influence are better candidates for the application due to their high SPA values.

I. INTRODUCTION

Considering the new biomedical strategies allowed by the use of magnetic nanoparticles (MNPs), such as drug delivery, bioimaging, biosensors, and magnetic fluid hyperthermia (MFH) [1], the knowledge and control of particle-intrinsic parameters, colloidal properties, and spatial arrangements are key for determining the MNP magnetic relaxation. Consequently, these parameters have a drastic effect on MFH as a cancer therapy, where the energy losses from colloidal MNPs under a high-frequency ac magnetic field are converted into heat. A measure of the performance of MNPs in MFH experiments is the specific power absorption (SPA), the power absorbed per unit mass

of MNPs. The SPA can be quantified as SPA $= Af$, with A the area enclosed by the magnetization hysteresis loop of the MNP system and f the frequency of the ac field in the MFH experiment. Thus, the area A is a direct measurement of the heating capability of a MNP system for a fixed experimental frequency f.

The optimization of the heating efficiency of MNPs is currently focused on the design of MNPs with tuned properties, for instance, their size Φ, saturation magnetization M_S, or effective magnetic anisotropy K. The dependence of the SPA with these particle-intrinsic parameters has been analyzed for different systems [2–6], and several synthetic routes have been systematized for this matter [7–9]. Another way of attacking the problem is to search for the optimal experimental conditions (ac field amplitude H_0 and frequency f) for a particular system [3,10]. Several

---

*debiasi@cab.cnea.gov.ar

attempts have been made to explain or predict the behavior of a MNP system using both experimental and theoretical approaches [11,12] as well as phenomenological models and simulations of simple systems to recognize the fundamental parameters that govern the SPA [13,14]. However, the problem of optimizing all parameters under general experimental conditions for MFH has not yet been solved.

Even with particle-intrinsic parameters and experimental conditions determined for optimal heating, the effects of interparticle interactions occurring in actual MFH experiments are not yet completely understood. It is well known that interparticle interactions in MNP aggregates can drastically change the performance when compared with a perfectly dispersed system [15–20]. The majority of *in vitro* tests do not reflect the SPA performance predicted from the characterization of MNPs in a ferrofluid, in part due to the high viscosity of the intracellular medium (with viscosity $\eta \approx 50 - 140 \, \text{mPa s}$) [21,22] in comparison to water ($\eta \approx 0.4 - -1 \, \text{mPa s}$) [23], but also due to the agglomeration promoted by cellular incorporation (which increases the hydrodynamic volume V_h) [23]. These effects produce an increment in Brown's relaxation time $\tau_B = 3\eta V_h/k_B T$, with k_B the Boltzmann constant and T the temperature. Under viscosities similar to those of the intracellular media Brown's relaxation mechanism, involving the coherent rotation of the MNP and its magnetic moment, is abrogated and the main contribution is the reversal of the magnetic moment through Néel relaxation [24,25].

Recently reported works show that interparticle interactions modify the relaxation time or blocking temperature [26–28] and explore the influence of MNP assemblies on the hysteresis loops' area or SPA [29,30], while others analyze heat dissipation in agglomerated system [31]. Despite the wide variety of works and approaches on the subject, there is still some controversy on the influence of interactions on the SPA of MNP systems. Both beneficial and detrimental effects on the SPA have been reported, when compared with the dispersed noninteracting case [18,32–42]. This dissent could originate in the great variety of agglomerates, since dipolar interactions strongly depend on the spatial configuration of the MNPs. Even for the specific case of linear agglomerates (i.e., chains of MNPs), there is some controversy, with reports attributing SPA values in chains that are lower [43–45] and higher [18,38–40, 46,47] than the noninteracting case. Recently, we reported theoretical results on the beneficial role of dipolar interactions on the SPA of an ideal chain structure of interacting MNPs with a relatively low anisotropy field [47], that was subsequently confirmed through experiments [20].

This work aims to describe the behavior of the hysteresis loops for MNP systems under ac magnetic fields, in conditions usually applied to MFH, as a function of relevant particle-intrinsic parameters, typical experimental conditions and interactions (added in the form of linear arrangements). The main focus will be given to the enclosed area of the magnetization hysteresis loops (i.e., the SPA) as a function of relative anisotropy $h_K = H_K/H_0$ (with H_K the anisotropy field and H_0 the amplitude of the ac field), which unravels different "regions." These regions where the systems can be placed determine the outcome of a MFH experiment and are therefore a powerful tool for the targeted design of MNPs and the control of their SPA. Moreover, our work deepens the understanding of the dipolar interaction role in MFH experiments by modeling an ideal MNP chain system and analyzing a wide range of particle-intrinsic parameters, confirming that the debate regarding the beneficial or detrimental effect of dipolar interactions can be understood when comparing the effective coercivity H_C^{eff} with the amplitude of the MFH ac field H_0. We expand the results presented in our previous work [47] by analyzing a wide range of relative anisotropies. Furthermore, we provide an analytical approach to the problem and its validity range, tools that help to predict the optimal systems and MFH conditions and to comprehend experimental results.

This paper is organized into four sections. Section I is the present introduction, and Sec. II resumes the main aspects of our model. In Sec. III, we present and discuss our results (with four subsections: noninteracting case, interacting case, analytical approach, and randomly oriented MNPs and chains) and we finally highlight the key ideas of the study in Sec. IV.

II. THE MODEL

Previously, we developed a model that describes the ac hysteresis loops of noninteracting MNPs and interacting linear chain systems under ac fields with amplitude H_0 and frequency f in the usual MFH range [48,49]. In a separate analysis [47], we treated these MNP systems in the low-anisotropy regime (i.e., $H_K < H_0$) only. Here, we cover a wider range of anisotropy values. In this way, we do not only complement the aforementioned study but we also build up a tool that allows the design of systems with specific properties and experiments with certain conditions to optimize the SPA.

Full details on the model can be found in Ref. [47]. Here, we summarize the key aspects of it to provide the reader with a self-contained study. Our model is probabilistic, and its main highlights are the incorporation of temperature, frequency, anisotropy, and interaction effects into the magnetic relaxation.

A. Noninteracting case

We assume a single-domain spherical MNP with uniaxial effective anisotropy oriented at an angle ϕ_n with respect to the external field **H**, whose magnetic relaxation time τ is determined by Néel's mechanism. The energy E of a MNP can be written through the Stoner-Wohlfarth model [50]

that yields two minima

$$E = -\mu_0 \boldsymbol{\mu} \cdot \mathbf{H}_{\text{loc}} - KV(\hat{\mathbf{n}} \cdot \hat{\boldsymbol{\mu}})^2, \qquad (1)$$

where μ_0 is the vacuum permeability, $\boldsymbol{\mu}$ the magnetic moment of the MNP, K its anisotropy constant and V its volume, and $\hat{\mathbf{n}}$ denotes the direction of the easy axis. The local field $\mathbf{H}_{\text{loc}}$ is equal to $\mathbf{H}$ in the noninteracting case.

In our approach, each MNP represents an ensemble of MNPs in which a fraction P_0 of the ensemble is in one minima and P_1 in the other. These fractions or "populations" P_k, $k = 0, 1$, can change over time because there is a probability $L = L(H, T_{\text{exp}}, \tau_m) = 1 - \exp(-\tau_m/\tau)$ that a MNP can fluctuate between the two minima, where T_{exp} is the temperature of the experiment and τ_m the measurement time. The time evolution of the populations of the minima is given by [51]

$$P_0(t + \delta t) = P_0(t) + L[P_0^\infty - P_0(t)], \qquad (2)$$

where P_0^∞ is the equilibrium population associated with the energy minimum 0 and δt the time discretization. As our model is probabilistic, to calculate the average magnetization of the system $\langle \mu \rangle = \langle \boldsymbol{\mu} \cdot \mathbf{H} \rangle$ we need to consider both the superparamagnetic $\langle \mu \rangle_{\text{SP}}$ and blocked contributions $P_k \langle \mu \rangle_{Bk} = P_k \langle \boldsymbol{\mu} \cdot \mathbf{H} \rangle_{Bk}$ (with $k = 0, 1$) in the ensemble with probabilities L and $1 - L$, respectively. The average magnetization due to the superparamagnetic fraction comes from the integration over all microstates of the system, while for the blocked averages, it comes from the integration in the corresponding minima region. In this way, the total average magnetization of the system $\langle \mu \rangle$ as a function of t is [51]

$$\langle \mu \rangle = L\langle \mu \rangle_{\text{SP}} + (1 - L) \sum_{k=0,1} P_k \langle \mu \rangle_{Bk}, \qquad (3)$$

where the time dependence is given through the evolution of the minima population described by Eq. (2) and the changes in the minima due to the external field.

B. Interacting case: linear chains of MNPs

We assume a chain of equally spaced single-domain spherical MNPs whose magnetic relaxation is predominantly given again by Néel's mechanism. The uniaxial effective anisotropy axes are aligned in the direction of the chain, at an angle ϕ_n with respect to $\mathbf{H}$ (indicating, in this case, the "orientation" of the chain). Each MNP interacts dipolarly with all MNPs in the same chain, but they do not interact with neighbor chains, meaning that we can accurately describe diluted chain systems that are not affected by collective behavior (typical in highly compact agglomerates) [52–54]. The complete implications of our hypotheses are detailed in Ref. [47].

Two differences between the chain and the noninteracting cases must be noted. First, despite that the energy of a MNP is again described by Eq. (1), the local field on the MNP is now given by $\mathbf{H}_{\text{loc}} = \mathbf{H} + \mathbf{H}_{\text{dip}}$, with $\mathbf{H}_{\text{dip}}$ the dipolar field generated by the other MNPs in the chain. Second, the statistical average of the magnetic moment of a MNP now has a component parallel to $\mathbf{H}$, $\langle \mu^\parallel \rangle = \langle \boldsymbol{\mu} \cdot \mathbf{H} \rangle$ and a perpendicular one $\mathbf{H}$, $\langle \mu^\perp \rangle$. Both of these averages need to be calculated as in Eq. (3) (see Ref. [47]).

C. Details on the numerical calculations

It is useful to detail some of the implementation procedures related to the correct use of our model. As detailed in Ref. [47], for the interacting case, the dipolar field on each MNP at time $t + \delta t$ is calculated with the magnetic configuration at time t. When every single MNP has been treated this way, we update the magnetic configuration corresponding to $t + \delta t$. In this way, we ensure that the results do not depend on the order in which the state of the MNPs is updated.

To correctly calculate the SPA of a given system or the equivalent enclosed hysteresis area for a simulated MFH experiment, it is necessary to take into account that we are calculating the time average of the desired quantity (on a time scale much greater than that associated with the frequency of the experiment). In the case where $H_K < H_0$, magnetization always reaches thermodynamic equilibrium, and then, the average enclosed area is equal to that of an individual loop. However, when $H_K \gg H_0$, the minor loops do not reach thermodynamic equilibrium, but the system does reach dynamic equilibrium after successive cyclings [55]. To ensure dynamic equilibrium is reached in simulations, we compare the magnetization in the maximum field value in the current cycling $M(H_0)$ and the previous one $M_0(H_0)$, and we continue cycling until the tolerance $[M(H_0) - M_0(H_0)]/M_0(H_0) = 1 \times 10^{-5}$ is reached.

III. RESULTS

Our analysis covers a wide range of parameters, making it quite general and valid for different materials widely used in MFH experiments such as the ferrites. The value of saturation magnetization $M_S = 3.5 \times 10^5 \, \text{A m}^{-1}$ is fixed and corresponds to maghemite particles [56]. Iron oxide nanoparticles are of great interest for MFH applications as they are known to be biocompatible and chemically stable [57,58] and approved by the FDA for clinical applications [59–61]. All parameter values are given at $T \to 0$ and temperature effects are naturally incorporated by our model's formulation.

All simulations are performed for room temperature $T_{\text{exp}} = 300$ K, to mimic the initial temperatures in a MFH experiment. An ac field with an amplitude of $H_0 = 16 \, \text{kA m}^{-1}$ is used, which is typical in MFH experiments

[29,49], although we normalize all field quantities. Unless stated otherwise, the frequency used for the simulations is $f = 100$ kHz, and the orientation of the anisotropy axes with respect to the external ac magnetic field is $\phi_n = 0$. We analyze different f and ϕ_n values in Secs. III A 2 and III D, respectively. For magnetization hysteresis loops, we present them as normalized magnetization m versus normalized magnetic field h curves, where the magnetization is normalized by M_S and the field by the corresponding anisotropy field $H_K = 2K/(\mu_0 M_S)$. Under these conditions, the MNPs are in the superparamagnetic regime in typical dc measurements and in the blocked regime in MFH conditions at zero field.

A. Noninteracting case

To start exploring the problem, we simulate the magnetization hysteresis loops for systems constituted by noninteracting MNPs with diameter $\Phi = 60$ nm and different relative anisotropy fields $h_K = H_K/H_0$. Although the value of Φ is somewhat larger than the MNP size generally used in MFH experiments, we choose it as an idealized system to understand the limit where thermal fluctuations are almost negligible (see Secs. III A 1 and III A 3), regardless of the possibility of finding single-domain MNPs of that size. In this way, it can be used as a starting point to understand what happens for other particle sizes in which the interpretation is not as straightforward, thus making it simpler. To assess the heating efficiency of this system, the area A of the loops (normalized by the number of MNPs in the system, N) is evaluated. Taking into account that for $T \to 0$ the largest major hysteresis loop is rectangular and has an area $A_0 = 4\mu_0 M_S V H_0$, we present all area values as normalized area $a = A/A_0$.

In Fig. 1, the curve a versus h_K for MNPs with diameter $\Phi = 60$ nm is presented. This curve has four clearly discernible regions identified from I to IV with increasing h_K and is referred to as the "area curve" of the system hereafter. Qualitatively, for low relative anisotropy values, it starts off with a being nearly zero (region I) and then grows linearly with h_K (region II) until it reaches a maximum when the coercive field H_C equals the field amplitude H_0. The hysteresis loop corresponding to the condition $H_C = H_0$ can be seen in the inset of Fig. 1. Above this condition, for higher relative anisotropies, a decreases abruptly (region III) to an almost null value (region IV). Monte Carlo simulations performed by Serantes *et al.* [41,62] yield results compatible with our observations.

Representative hysteresis loops at each region (for the h_K values indicated with crosses in Fig. 1) provide an interpretation regarding what is happening to the MNP system as its relative anisotropy h_K changes and can be seen in Fig. 2. In region I, where magnetic anisotropy is low, almost no hysteresis is exhibited [Fig. 2(a)] because the thermal energy is of the order of the energy barrier.
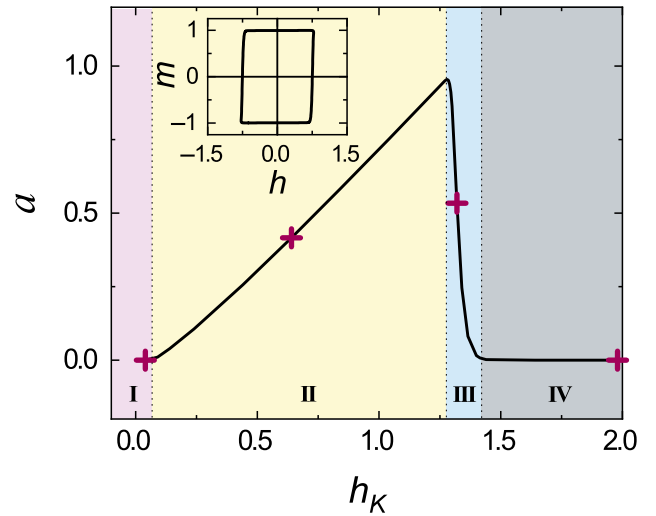

FIG. 1. Normalized hysteresis area a as a function of the relative anisotropy field h_K of a noninteracting MNP system with diameter $\Phi = 60$ nm and anisotropy axes parallel to the external field ($\phi_n = 0$) for a frequency $f = 100$ kHz. Crosses indicate h_K values where the loops in Fig. 2 are simulated. The inset shows the loop corresponding to the maximum of the area curve. Regions I to IV are indicated by colored zones in both panels.

In region II (moderate anisotropy values), the energy barrier increases above the thermal energy and the MNPs are not able to thermally fluctuate between energy minima at $H = 0$. Since the hysteresis loops in this region have a nearly rectangular shape [Fig. 2(b)], their area becomes proportional to the coercive field H_C and therefore increases linearly with the anisotropy constant K (see Fig. 1). For the condition $H_C = H_0$, the system reaches the maximum SPA, defining the maximum h_K^{opt} in the a versus h_K curve in Fig. 1.

For larger h_K values, which yields $H_C > H_0$, the system presents minor hysteresis loops. For regions III and IV, the applied magnetic field cannot invert all the magnetic moments and hysteresis is quickly lost. This yields an abrupt drop in the area of the hysteresis loops in region III [see Fig. 2(c)] until only a minute fraction of the magnetic moments of the system is able to switch minimum. This produces a loop with a very small but nonzero enclosed area for region IV [see Fig. 2(d)].

1. Area curves for different MNP diameters Φ

The case of MNPs with diameter $\Phi = 60$ nm discussed above, i.e., the value assumed as a lower limit for "large" MNPs, shows clear boundaries between regions with different magnetic behaviors under ac magnetic fields. In Fig. 3, the area curves (a versus h_K) for dispersed, noninteracting MNPs with diameters $\Phi = 5, 30$, and 60 nm are presented. By comparing Figs. 3(a)–3(c), it can be noticed that all the curves obtained are qualitatively similar: they exhibit four regions with a maximum area
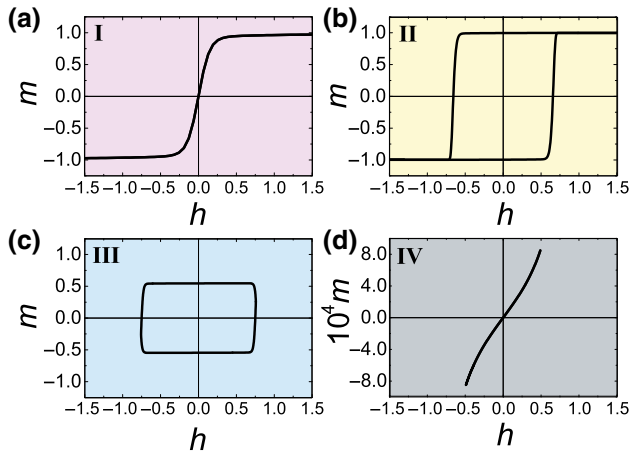
FIG. 2. Representative magnetization hysteresis loops for different regions (i.e., different values of h_K) of a noninteracting MNP system with diameter $\Phi = 60$ nm and anisotropy axes parallel to the external field ($\phi_n = 0$) for a frequency $f = 100$ kHz. (a) Region I, (b) region II, (c) region III, and (d) region IV. The corresponding h_K values are marked in Fig. 1 with crosses.

for a single h_K value, h_K^{opt} (i.e., the optimal MNP performance in MFH). However, two differences from the $\Phi = 60$ nm case are clearly visible. On the one hand, as the diameter decreases, the area curve stretches toward greater h_K values. On the other hand, the maximum area reached for MNPs with $\Phi = 5$ nm is one order of magnitude lower than the maximum for the other MNP sizes. This implies that larger MNPs systematically yield higher optimal SPAs.

The h_K values for the maximum of the area curves decrease with larger MNP sizes, getting closer to 1: $h_K^{\text{opt}}(\Phi = 5 \text{ nm}) \approx 200$, going through $h_K^{\text{opt}}(\Phi = 30 \text{ nm}) \approx 2.14$, and finally $h_K^{\text{opt}}(\Phi = 60 \text{ nm}) \approx 1.28$. For MNPs with $\Phi = 5$ nm, the curve is no longer asymmetric: it is bell shaped and symmetric with respect to its maximum. Moreover, in region II, a increases with h_K nonlinearly as a consequence of having major loops that are not rectangular; thus, A is no longer proportional to H_C [see the inset in Fig. 3(a)].

The linear response theory (LRT) [63] is valid under two fundamental assumptions that impose conditions on magnetic parameters [13]. The first condition is for the field amplitude H_0 to be much lower than the anisotropy field H_K, which guarantees that the position of both energy minima is given by anisotropy and that the effect of the applied field can be treated as a first-order perturbation, which implies a linear response of the system to the field sweep. The second condition is that $x = \mu_0 M_S V H_0 / k_B T \ll 1$, so that the equilibrium magnetization is linear with H (i.e., the "characteristic" Curie law of the superparamagnet is fulfilled). As in the LRT, in our nonlinear model, the dimensionless quantity x is also relevant because it measures the ratio between Zeeman and thermal energy.
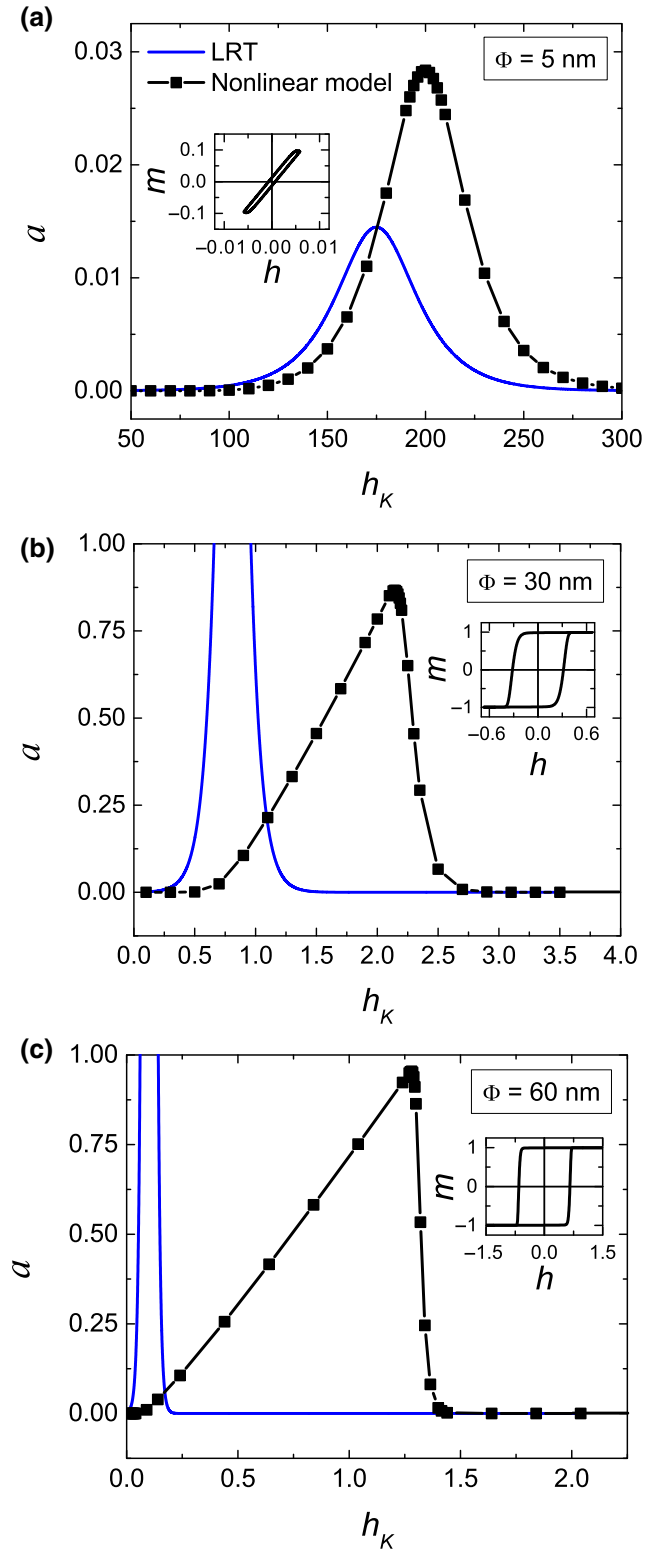

FIG. 3. Normalized hysteresis area a as a function of the relative anisotropy field h_K of a noninteracting MNP system with anisotropy axes parallel to the external field ($\phi_n = 0$) for a frequency $f = 100$ kHz and diameter (a) $\Phi = 5$ nm, (b) $\Phi = 30$ nm, and (c) $\Phi = 60$ nm. The curves for both our nonlinear model and the LRT are plotted. The insets show a representative loop in region II for each diameter.

However, our model has no limitations imposed on the value of x. It represents the relative preponderance of thermal fluctuations in the magnetic relaxation of the system. When $x \gg 1$ (i.e., thermal fluctuations are negligible with respect to $\mu_0 M_S V H_0$), the system behaves as in the limit of $T \to 0$. The optimal loop for MFH is perfectly rectangular with the coercive field equal to the amplitude of the applied ac field ($H_C = H_0$) and, as $T \to 0$, $H_C(T) \to H_K$. In this limit, the position of the maximum of the a versus h_K curve is then $h_K^{\mathrm{opt}} = 1$. For lower x values, thermal fluctuations become increasingly relevant and $H_C(T) < H_K$, which is the reason why the optimal loop is reached for $H_K > H_0$, and thus, $h_K^{\mathrm{opt}} > 1$.

The effects of thermal fluctuations on the magnetic relaxation can therefore explain the differences we have just noted in the curves in Fig. 3. Decreasing values of Φ imply decreasing values of x. In fact, $x(\Phi = 60 \text{ nm}) = 191.23$, $x(\Phi = 30 \text{ nm}) = 23.90$, and $x(\Phi = 5 \text{ nm}) = 0.11$. A lower x value implies an increasingly dominant role of thermal fluctuations, which are also reflected in the more round-shaped hysteresis loops when going from 60- to 5-nm MNPs (see insets in Fig. 3). Consequently, the relative enclosed area a is no longer proportional to h_K for major loops in region II when decreasing x, making the curve smoother (or bell shaped, as we describe before). Additionally, $H_C(T) < H_K$ for small x, which implies that the maximum of the curve (given by $H_C = H_0$) is shifted to a larger $h_K = H_K/H_0$ value and the range of the curve is expanded.

It is worth noting that the same analysis could have been done for fixed size Φ and different M_S values, as the parameter that reflects how much thermal fluctuations affect the relaxation is $x = x[M_S, V(\Phi)]$. However, as x is particularly sensitive to Φ (because it depends on the MNP's volume), we prefer this analysis that allows the use of a M_S significative for MFH application.

For comparison, the area curves for the same MNP systems obtained using the LRT [through Eq. (6) in Ref. [63]] are also displayed in Fig. 3. As mentioned above, the validity of this model is restricted to the $x \ll 1$ and $h_K \gg 1$ conditions, which are satisfied only for the system with $\Phi = 5$ nm ($x = 0.11$) under the (H_0, f) conditions used for the entire h_K range analyzed [see Fig. 3(a)]. This explains why the curves obtained through both models are similar in shape and predict near optimal conditions ($h_K^{\mathrm{opt}} \approx 200$ and $h_K^{\mathrm{opt\ LRT}} \approx 175$) for the MFH experiment. For larger MNPs, the LRT requirements are no longer satisfied [$x > 1$ for systems in Figs. 3(b) and 3(c)] and the corresponding LRT data are completely different, not only in shape but also in magnitude. It is worthwhile to note that the description of a system employing the LRT when the hypotheses of the model are not attained has drastic consequences, since the predicted area sometimes exceeds the maximum area of a perfectly rectangular loop ($a > 1$), which cannot be possible.

2. Area curves for different experimental frequencies f

The previous section dealt with the evolution of the area curve under a fixed experimental frequency ($f = 100$ kHz), which is close to the clinical values currently accepted in MFH. However, a large amount of *in vitro* experimental works have reported the use of higher frequencies of up to 1 MHz [48,49], and therefore we extend our analysis to cover this frequency range. The curves a versus h_K for $f = 100$ kHz and 1 MHz and different MNP sizes are shown in Fig. 4. The area curves are qualitatively similar, with the same four regions separated by clear boundaries, but slightly shifted to lower h_K values when f is increased. The shift is considerable and nonnegligible only in the case of $\Phi = 5$ nm and can also be interpreted as an effect of thermal fluctuations on the magnetic relaxation of the system. Increasing the frequency implies reducing the measurement time τ_m with respect to the relaxation time τ of the MNPs, thus diminishing the thermal fluctuations of the magnetic moments during the measuring time of the experiment.

As discussed in Sec. III A 1, reducing thermal fluctuations produces a shift of the maximum to lower h_K values, as displayed in this case. As expected, the relative shift between the curves for both frequencies is larger for smaller MNPs since their magnetic moments are more susceptible to fluctuate due to the smaller energy barrier. In fact, the frequency shift when going from 100 kHz to 1 MHz is approximately equal to 20% for $\Phi = 5$ nm, approximately equal to 10% for $\Phi = 30$ nm, and approximately equal to 5% for $\Phi = 60$ nm.

We remark that, although there are no significant frequency-dependent changes in the area curves (specially for the $\Phi = 60$ nm case), the SPA is proportional to f. This means that under the frequency change from $f = 100$ kHz to 1 MHz the SPA is expected to increase. However, due to limitations set forth by the therapeutic use of MFH, the magnitude of $H_0 f$ should be reduced [64,65], thus lower frequencies are preferred.

3. Maximum of the area curves

Our previous results clearly show that the optimal condition, of maximum SPA, occurs at the boundary between regions II and III (i.e., the maximum of the area curve), where $H_C = H_0$. Following the position (h_K^{opt}) and magnitude ($a_{\max}$) of the maximum of the area curve for systems with different MNP diameters Φ, which imply different values of the magnitude x, we obtain the results shown in Figs. 5(a) and 5(b), respectively. In Fig. 5(a) we can see that for small MNPs (in terms of x), large relative anisotropy values are needed to reach optimal conditions and, as we note before, $h_K^{\mathrm{opt}} \to 1$ when $x \gg 1$ due to diminishing the effects of thermal fluctuations on the coercivity of the hysteresis loops. This gives us a "saturating"
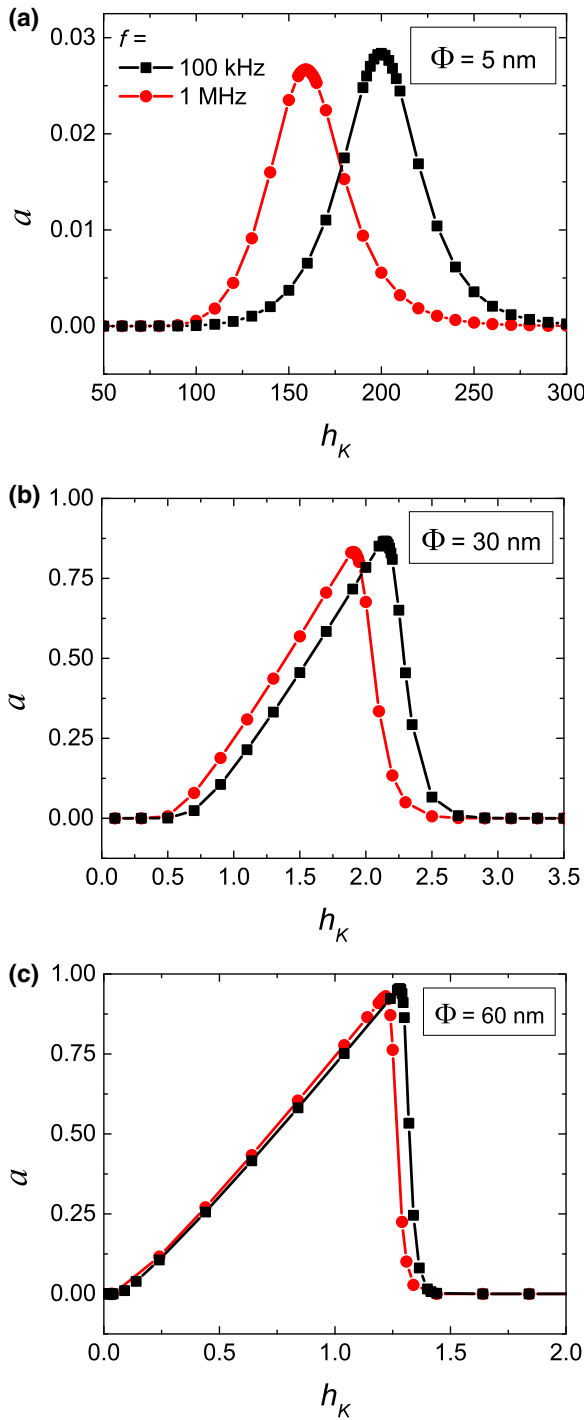
FIG. 4. Normalized hysteresis area a as a function of the relative anisotropy field h_K of a noninteracting MNP system with anisotropy axes parallel to the external field ($\phi_n = 0$) and diameter (a) $\Phi = 5$ nm, (b) $\Phi = 30$ nm, and (c) $\Phi = 60$ nm for different MFH frequencies f.

zone from $x \approx 10$ onward, where we can assume thermal fluctuations do not affect the relaxation significantly.

For a given x, the noninteracting system with the highest SPA at fixed experimental conditions (H_0, f) will be the
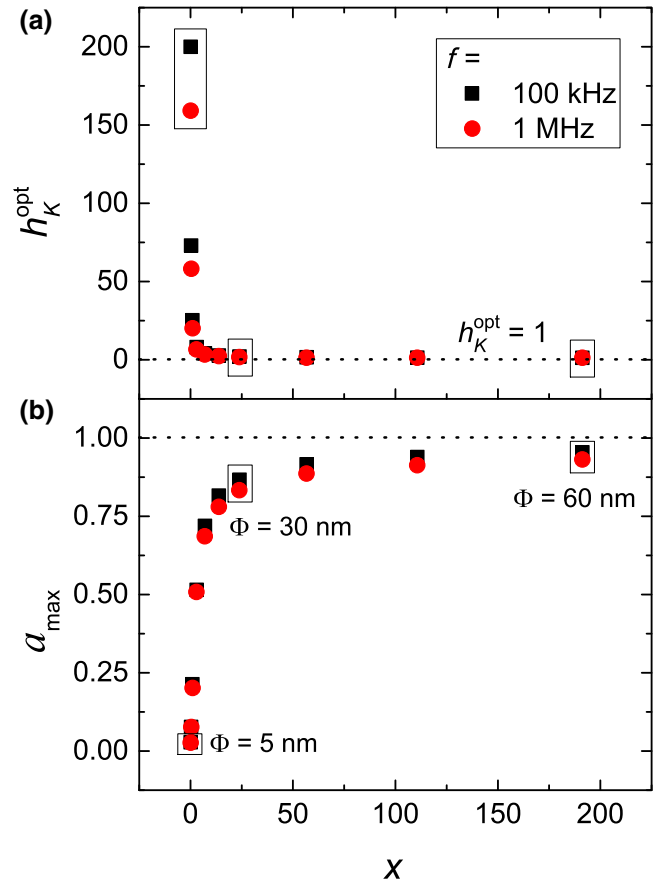

FIG. 5. (a) Position of the maximum of the area curves h_K^{opt} and (b) maximum dimensionless area $a_{\max}$ as a function of $x = \mu_0 M_S V H_0 / (k_B T)$. The results are shown for extreme MFH working frequencies. Dotted lines represent the values given for the $T \to 0 / x \gg 1$ cases.

one with anisotropy constant $K^{\mathrm{opt}}(x) = h_K^{\mathrm{opt}}(x)\mu_0 M_S H_0/2$. As region III implies a sudden decrease in the SPA, if the optimal anisotropy K^{opt} is not reachable through the chosen synthesis method, it is better to have $K < K^{\mathrm{opt}}$ (i.e., a system in region II).

Regarding the magnitude of the maximum $a_{\max}$ as a function of x, we see a "saturating" behavior toward $a_{\max} = 1$ that is the maximum normalized area value, which is characteristic of a rectangular hysteresis loop $2H_0$ wide and $2\mu_0 M_S V$ high. It can be noticed that MNPs with diameters of $\Phi = 30$ nm are in the "saturating" part of the curve, so we can describe them as a system where thermal fluctuations are not relevant to the magnetic response. Here we can finally see the usefulness of analyzing $\Phi = 60$ nm MNPs: they are more intuitive and can help us to easily understand results for $\Phi = 30$ nm, which is more relevant for the application. However, the loops for MNPs with diameter $\Phi = 5$ nm are greatly affected by these fluctuations and their behavior is not as predictable as the other two.

B. Interacting case: linear chains of MNPs

To analyze the actual conditions in MFH experiments, in which some degree of MNP agglomeration is unavoidable [23], we also perform simulations that include the effect of dipolar interactions among MNPs. We choose a simple MNP configuration but relevant for the MFH application: ideal chains of identical and equally spaced MNPs. Indeed, it has been shown that linear arrangements can drastically change MNP heating performance in MFH experiments. However, both theoretical and experimental results in the literature are contradictory as linear arrangements have been found either to increase or decrease the SPA with respect to noninteracting MNPs [18,38–40,43–47].

First, we present results for chains with easy axes oriented parallel to the external field ($\phi_n = 0$). The randomly oriented axes are analyzed in Sec. III D. We simulate chains of $N = 25$ MNPs in all cases, since in a previous study, we have determined that the area (normalized by N) and coercivity of the hysteresis loops already saturates for this length [47]. We consider chains of MNP with different diameters Φ fixing the ratio $\Phi/d = 0.5$, where d is the interparticle distance, so that the dipolar field between neighboring MNPs with $x \gg 1$ is the same for all systems, irrespective of Φ [see Eq. (4) for clarification].

In Fig. 6, the area curve for the interacting chain of MNPs is compared with that of a noninteracting system for different diameters. Although we fix the magnitude Φ/d so that the dipolar field acting on a MNP with $\Phi = 5$ nm at a given position in the chain is close to the value for a MNP with $\Phi = 60$ nm at the same position (strictly true only at saturation), the behavior of the area curves shown in Fig. 6 varies with the different MNP sizes: while chains with smaller MNPs show an area curve nearly identical to the noninteracting case (also reflected in the hysteresis loops), interactions affect the results for larger MNPs.

In Sec. III A 3, it is shown that MNP systems with $\Phi = 5$ nm are greatly affected by thermal fluctuations (due to their small x value). Instead, for systems with $\Phi = 30$ and 60 nm [larger x, in the "saturating" zone in Fig. 5(a)], thermal-fluctuation effects are negligible and interactions dominate the relaxation. Interactions then shift the hysteresis area curve corresponding to the interacting MNP system towards lower h_K values in comparison to the noninteracting area curve.

As presented in Ref. [47], dipolar interactions in chains produce a shift between the local and the applied field on a MNP, which can be translated into an increase of the effective relative anisotropy h_K^{eff} of the system. Furthermore, this shift can explain the apparent controversy that originated in publications on linear MNP systems that state that interactions are beneficial or detrimental to the SPA with respect to the noninteracting case. If we look at the area curves for MNPs with $\Phi = 30, 60$ nm, there is a h_K range where a (i.e., the SPA) of the interacting system is larger than that of the noninteracting, dispersed
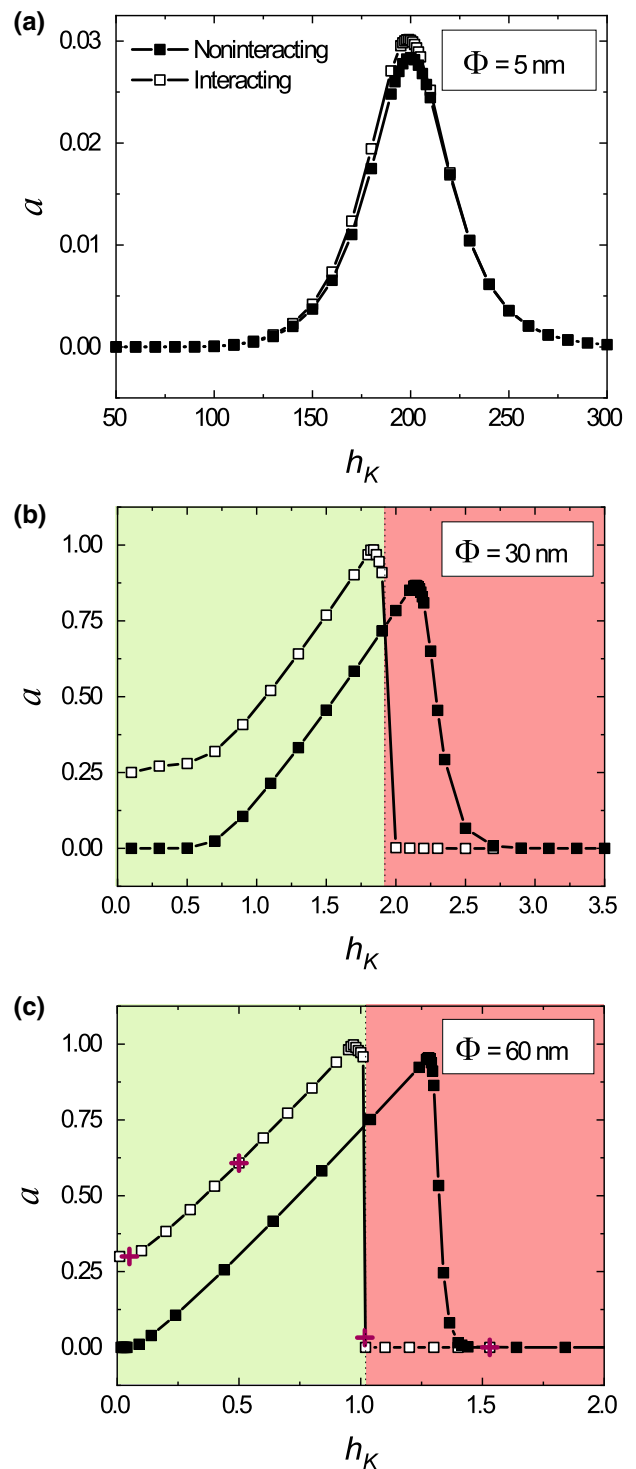

FIG. 6. Normalized hysteresis area a as a function of the relative anisotropy field h_K for a noninteracting MNP system and an interacting chain of MNPs, both with anisotropy axes parallel to the external field ($\phi_n = 0$), experimental frequency $f = 100$ kHz, and diameter (a) $\Phi = 5$ nm, (b) $\Phi = 30$ nm, and (c) $\Phi = 60$ nm. The ratio between diameter and interparticle spacing is fixed in $\Phi/d = 0.5$. The green-colored (red-colored) zones represent the h_K range where interactions present a beneficial (detrimental) effect on the SPA. Crosses indicate h_K values where the loops in Fig. 7 are simulated.

system [the beneficial effect, colored green in Figs. 6(b) and 6(c)] and another h_K range where the SPA of the interacting system is lower or equal to that of the noninteracting case [the detrimental effect, colored red in Figs. 6(b) and 6(c)]. Another consideration to have in mind is that, for a fixed h_K, the noninteracting and interacting systems with anisotropy constant K do not always belong to the same region, which implies that agglomeration can result in a MNP system quite different to the noninteracting one due to switching from one region to another.

However, we note that the effect of interactions is not a mere shift, since there are some clear differences with respect to the noninteracting case for chains of larger MNPs ($\Phi = 30, 60$ nm). First, region I reaches a nonzero "plateau" contrarily to the noninteracting case (where the area value in this region is zero due to MNPs being nearly in the superparamagnetic regime). Second, region III becomes narrower in terms of h_K range. Region II looks very similar, also showing a linear behavior $a \propto h_K$; however, the linearity range diminishes slightly.

Figure 7 shows representative hysteresis loops for each of the four regions for the interacting system of chains composed by MNPs with diameter $\Phi = 60$ nm [see Fig. 6(c) for the area curve, with the corresponding h_K values indicated by crosses]. When comparing these loops with the loops in Fig. 2, we notice that the differences come from regions I and III. Region II continues to exhibit rectangular major loops, and region IV loops continue to have an infinitesimal enclosed area. However, loops corresponding to region I now have a coercivity, and region III presents minor loops that are neither symmetrical nor centered on the origin (a similar result has already been shown

by Serantes *et al.* [41], also for linear aggregates). This off-centered loop is produced by the contribution from H_{dip}, helping the external field to anchor moments at the favored minimum and thus producing a population imbalance in the cycling that cannot be reversed. In Appendix A, a more detailed explanation of this phenomenon is presented.

To explain the differences between interacting and non-interacting cases (the "shift" of the area curves towards lower h_K values, the "plateau" in region I and the more pronounced drop of region III for the interacting case), we need to consider the dispersion of dipolar fields for MNPs in different positions in the chain. We cover all of these aspects by considering the case of $\Phi = 60$ nm that can be approached through $x \gg 1$ formulas due to thermal fluctuations being negligible in this case. In this way, the relative dipolar field $h_{dip j} = H_{dip j}/H_0$ on the jth MNP in a chain with easy axes parallel to the external field and $x \gg 1$ can be estimated as

$$h_{dip j}(x \gg 1) \sim \frac{\pi}{3} \frac{\mu_0 M_S}{H_0} \left(\frac{\Phi}{d}\right)^3 \sum_{i \neq j} \frac{1}{|i - j|^3}. \quad (4)$$

Note that by considering different values of j (i.e., different MNPs or positions in the chain), we obtain different values of dipolar field, namely, the aforementioned dispersion of dipolar fields. For our particular case, taking into account the length of the simulated chains, the calculated dipolar field [by Eq. (4)] on the MNP at the border of the chain results in $h_{dip border}(x \gg 1) = 0.28$ and at the center of the chain $h_{dip center}(x \gg 1) = 0.55$ (in agreement with simulations, data not shown). This means that the MNPs at the border of the chain will have a lower $|H_{loc}|$; thus, they will be the first to invert their magnetic moments. As this happens, it lowers $|H_{dip i}|$ on the neighboring MNPs, and they invert their moments "in cascade." This fact explains the narrower h_K range observed for region III in the interacting case and makes the effective coercive field of the chain very close to the effective coercive field of the border MNP.

Considering that MNPs are almost in the superparamagnetic regime in region I, the relative effective coercivity h_C^{eff} of the loop in Fig. 7(a) should be given purely by the dipolar field and very close to the $h_{dip border}$ value we have just estimated. In fact, coercivity in this loop is $h_C^{eff} \approx 0.28$, matching both the calculated and simulated $h_{dip border}$ values.

The coercivity shown in region I is the origin of the nonzero "plateau" in the interacting area curves. In effect, the value of the plateau for chains with $\Phi = 60$ nm can be estimated with the aforementioned coercivity value by calculating the area of a loop $2H_C^{eff}$ wide and $2 \mu_0 M_S V$ high, giving $a_{plateau} = (2H_C^{eff} \mu_0 M_S V)/(2H_0 \mu_0 M_S V) = h_C^{eff} \approx 0.28$, which is coherent with the data displayed in Fig. 6(c). Moreover, the shift of the area curve with respect to the
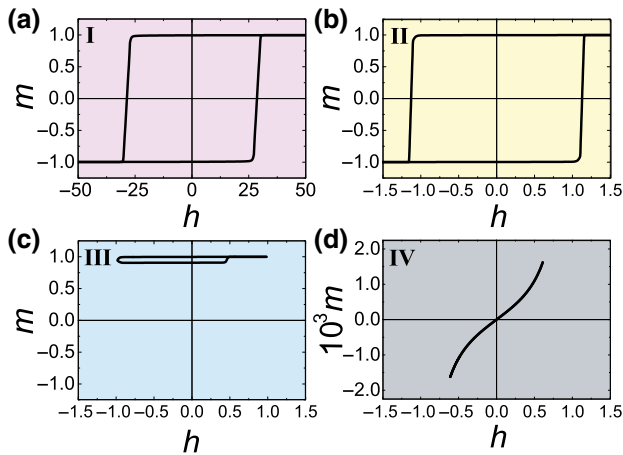

FIG. 7. Representative magnetization hysteresis loops for different regions (i.e., different values of h_K) of an interacting MNP chain system with diameter $\Phi = 60$ nm and anisotropy axes parallel to the external field ($\phi_n = 0$) for a frequency $f = 100$ kHz. (a) Region I, (b) region II, (c) maximum, limit between regions II–III, (d) region III, and (e) region IV. The color of each panel references the regions, as in Figs. 1 and 2.

noninteracting one taken from the simulated data is $h_K^{\mathrm{eff}} - h_K \approx 0.3$, which is very close to the "plateau" value due to $H_C(T) \sim H_K$ for a system where thermal fluctuations are negligible.

1. Maximum of the area curves

As we did for the noninteracting case, we can follow the position and magnitude of the maximum of the area curve for chain systems with different MNP diameters Φ that imply different values of the magnitude x. The results can be seen in Figs. 8(a) and 8(b). As we inspect them, we realize that the tendencies are quite similar to those for the noninteracting case (displayed in dashed lines for comparative purposes): as x increases, the optimal relative anisotropy h_K^{opt} decreases by 2 orders of magnitude and
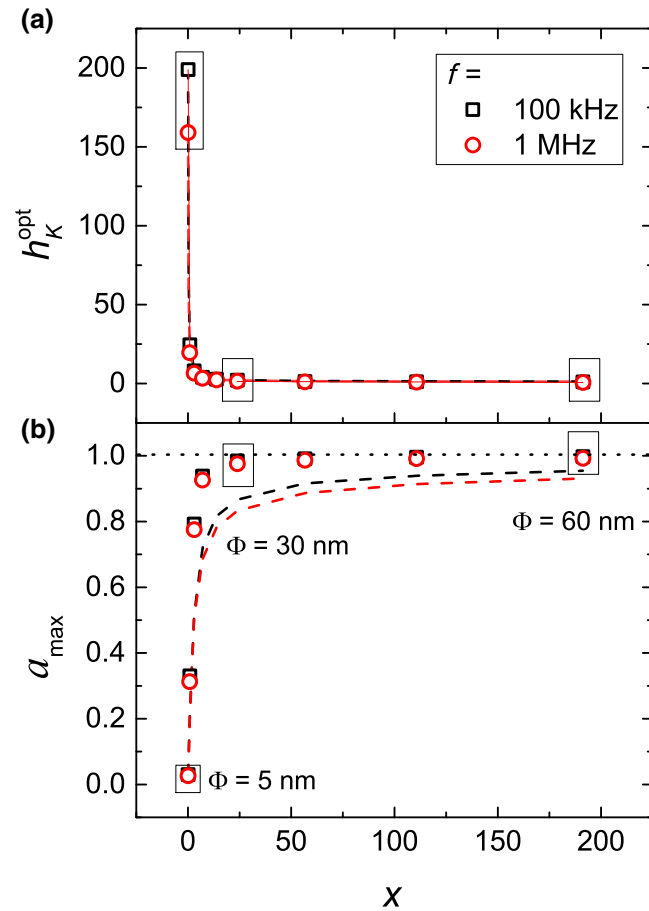

FIG. 8. (a) Position of the maximum of the area curves h_K^{opt} and (b) maximum dimensionless area $a_{\max}$ as a function of $x = \mu_0 M_S V H_0/(k_B T)$ for MNP chain systems with anisotropy axes parallel to the external field ($\phi_n = 0$). The results are shown for extreme MFH working frequencies. Dashed lines are noninteracting data simulated at $f = 100$ kHz (black) and 1 MHz (red) that are plotted in Fig. 5. They are presented for comparison. The dotted line represents the maximum enclosed area value for a loop in the case of $x \gg 1$.

the maximum area $a_{\max}$ increases, exhibiting a "saturating" behavior. However, as we explain in Sec. III B, coercivity is modified by the dipolar field on the MNP at the border of the chain (due to the "cascade" effect). This causes h_K^{opt} to tend to different values when $x \gg 1$ (not necessarily to 1, as in the noninteracting case), depending on the interaction strength.

The "saturation" is given again by the effect of thermal fluctuations: at lower x values, thermal fluctuations are dominant, but as x grows, the interaction influence becomes larger. However, for the interacting case, "saturation" is faster than in the noninteracting case: it is reached for lower x values (i.e., the MNP size range with significative SPA is expanded) and is closer to 1 in the x values of interest (i.e., the SPA is enhanced).

C. Analytical approach

We previously state that in going from region II to region III, there is a transition from major [$h_C^{\mathrm{eff}}(T) \leq 1$] to minor loops [$h_C^{\mathrm{eff}}(T) > 1$], given by the decrease in the fraction of magnetic moments that can be reversed. This transition defines the maximum of the area curve, at the value h_K^{opt}. Identifying the position of this maximum is extremely helpful for the design of MNPs for the application and, although it can be located through simulations, an analytical method to estimate it can be quite useful.

In this section, we generate "maps" of magnetization inversion as a function of h_K and frequency f, for different MNP systems characterized by its value of $x = \mu_0 M_S V H_0/(k_B T)$. We label the systems with their diameter value Φ (5, 30, and 60 nm) but it is useful to keep in mind that the relevant parameter is x (0.11, 23.90, and 191.23, respectively). The maps allow us to confirm that the inversion of magnetization is in close relation to the h_K^{opt} values obtained through simulations [Figs. 5(a) and 8].

We base our analytical development in systems with $x \gg 1$, with rectangular hysteresis loops that reach their maximum area when $H_K \sim H_0$. In this condition, the problem of finding h_K^{opt} is reduced to considering the inversion of magnetization at a field $H = H_0$. For the ascending branch of a hysteresis loop, starting at $H = -H_0$ and increasing until $H = H_0$, the probability of inversion as a function of the external field is given by $\xi(H) = 1 - \exp[-\tau_m/\tau'(H)]$, where τ' is the effective time associated with magnetization relaxation from a metastable energy minimum to the absolute minimum (at $H > 0$). This time is given by $\tau'(H) = \tau_0 \exp[\Delta E(H)/k_B T]$, where $\Delta E(H)$ is the energy barrier that can be approximated in the vicinity of the inversion by considering the changes in the coercive field associated with thermal fluctuations and dipole interactions [$\mathbf{H}_C^{\mathrm{eff}}(\mathbf{T}) = \mathbf{H}_C(T) + \mathbf{H}_{\mathrm{dip\ border}}(T)$, see Appendix B]. Under these hypotheses the energy barrier can be approximated by $\Delta E = [H_C^{\mathrm{eff}}(T) - H_0]\mu_0 M_S V$ (see Appendix B), where the effective coercive field can be

estimated as [66]

$$H_C^{\text{eff}}(T) \approx \frac{2K}{\mu_0 M_S} \left[1 - \sqrt{\frac{k_B T \ln(2\tau_m/\tau_0)}{KV}} \right] + H_{\text{dip}}, \quad (5)$$

with $H_{\text{dip}} = 0$ for noninteracting cases and $H_{\text{dip}} = H_{\text{dip border}}(x \gg 1)$ for the interacting case, considering the modification of the coercivity through the dipolar field on the MNP in the border of the chain that we discuss in Sec. III B.

When the external field $H = H_0$ is sufficient to "beat" the effective coercive field, the MNPs will have a probability $\xi \approx 1$ of reversing the orientation of their magnetization. This probability ξ can be calculated for different particle sizes Φ as a function of the experimental frequency f and the relative anisotropy of the system h_K, yielding a diagram for each Φ that estimatively maps the optimal MFH conditions and parameters. The results for MNPs with $\Phi = 5, 30,$ and 60 nm are presented as color maps in Fig. 9, both for noninteracting MNP systems [see Figs. 9(a)–9(c)] and chains of interacting MNPs [see Figs. 9(d)–9(f)]. The position of the maximum of the area curves (h_K^{opt}) obtained from the simulation of the magnetization hysteresis loops is displayed for each f in yellow triangles.

In all of these diagrams, we distinguish two zones and an interface between them: a zone where the magnetization of the system can be inverted at $H = H_0$ ($\xi = 1$, in blue on the color map), another one where it cannot ($\xi = 0$, in red on the color map) and the transition between them ($0 < \xi < 1$, in white on the color map). However, there are some contrasting characteristics when comparing diagrams for different Φ values. The most notorious difference is the diagram's h_K range: for $\Phi = 5$ nm, the h_K values where this transition happens are larger than those for systems of $\Phi = 30$ or 60 nm. This effect is coherent with the area curves presented for different diameters in Sec. III A 1. Moreover, for $\Phi = 5$ nm MNPs, the interface is rather broad in terms of h_K, while for $\Phi = 30, 60$ nm, the interface is quite sharp. This illustrates the shape of the transition from region II to region III: broader for the bell-shaped area curve of $\Phi = 5$ nm MNPs and sudden for $\Phi = 30, 60$ nm (see Fig. 3).

If we compare the h_K^{opt} obtained for different f values in the MFH range through the complete simulation of the hysteresis loops of the systems (see yellow triangles in Fig. 9) with the interface values in these diagrams, we notice they are in agreement, especially for $\Phi = 30, 60$ nm. Notorious differences for smaller MNPs ($\Phi = 5$ nm) arise from the fact that, for this analytical approach, we are looking at
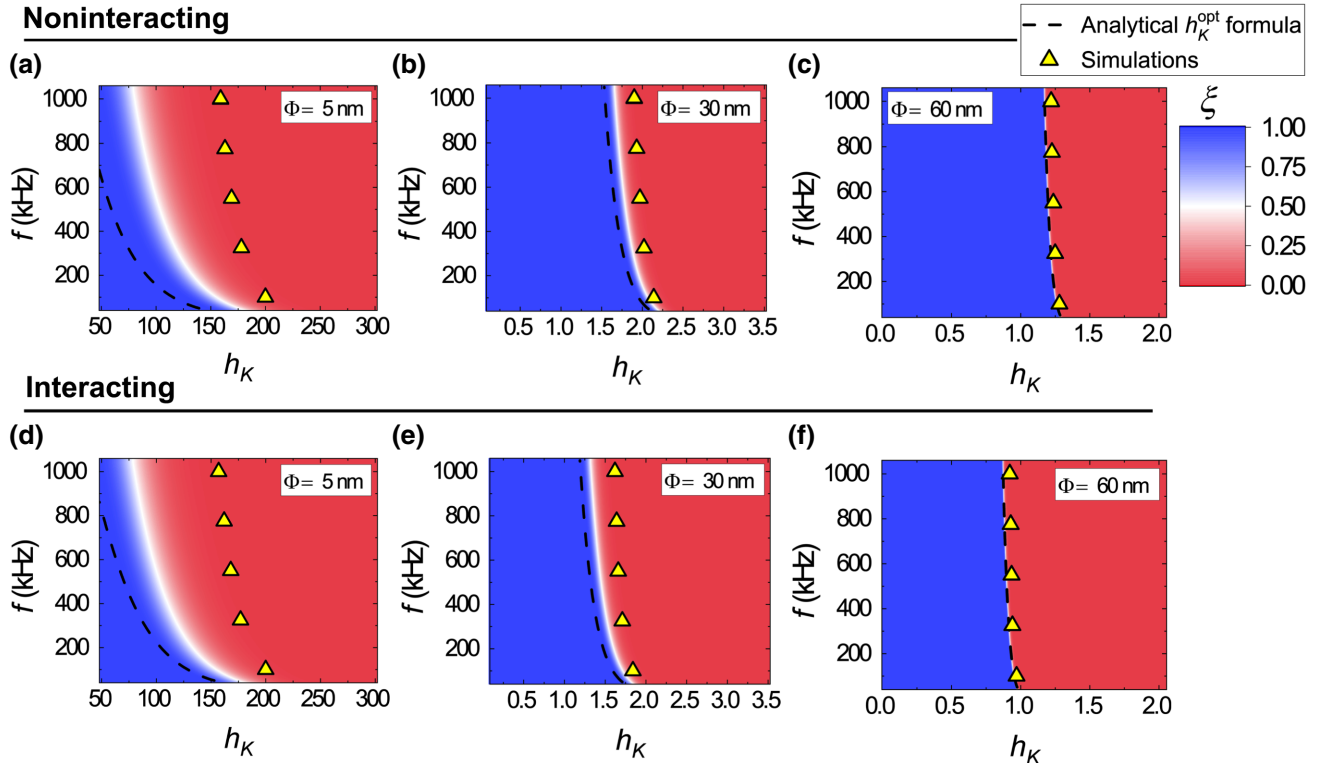

FIG. 9.   Probability ξ of reversing the magnetization at a field $H = H_0$ as a function of experimental frequency f and relative anisotropy h_K for several systems. Noninteracting MNPs with diameter (a) $\Phi = 5$ nm, (b) $\Phi = 30$ nm, (c) $\Phi = 60$ nm, and chain of interacting MNPs with diameter (d) $\Phi = 5$ nm, (e) $\Phi = 30$ nm, (f) $\Phi = 60$ nm. Both systems have anisotropy axes parallel to the external field ($\phi_n = 0$). For the interacting case, the ratio between diameter and interparticle spacing is fixed in $\Phi/d = 0.5$.

the effective coercive field of the loops [as can be inferred from Eq. (5)], not the enclosed area. As we already see in Fig. 3, for MNPs with diameter $\Phi = 30, 60$ nm the loops are almost rectangular [i.e., their area is proportional to $H_C^{\text{eff}}(T)$], while for $\Phi = 5$ nm loops are ellipsoidal [i.e., their area is no longer proportional to $H_C^{\text{eff}}(T)$], accounting for the differences.

Now, as we are considering an energy balance to calculate the probability ξ, in the diagrams we are looking at how all these terms play out. For example, for MNPs with diameter $\Phi = 5$ nm, there is a strong frequency dependence, not displayed in systems with larger Φ. However, when comparing the noninteracting and interacting diagrams for $\Phi = 5$ nm MNPs, no notorious change is exhibited. This accounts for the stronger thermal fluctuation influence on smaller particles. For larger MNPs, a "shift" of the interface towards lower h_K values (already discussed in Sec. III B) is caused by the addition of interactions.

As we mention in Sec. III A 1, larger MNPs yield a larger SPA. Moreover, we confirm that for these MNPs, a correlation exists between the analytically obtained interface and the h_K^{opt} simulated values. Therefore, we can actually predict the optimal MFH conditions for the MNP sizes that are more favorable for the application. The idea is to provide an analytical closed-form expression to calculate h_K^{opt} in the limit of low thermal fluctuations (i.e., for large x) as well as to determine the validity range of this approximation. Diagrams of probability ξ better fit simulations in cases of large x, where the interface (in white on the color maps) is exceptionally narrow. Because of this "sharp" transition of the probability ξ from 1 to 0, we are going to find the interface by considering a small decrease ϵ in the probability value (i.e., when $\xi = 1 - \epsilon$). Rewriting ξ as a function of x and rearranging

$$h_K^{\text{opt}} \approx 1 - h_{\text{dip}} + \frac{1}{x}\left[\ln\left(\frac{2\tau_m}{\tau_0}\right) + \ln\left(-\frac{\tau_m}{\tau_0 \ln\epsilon}\right) + \sqrt{\ln\left(\frac{2\tau_m}{\tau_0}\right)\left\{\ln\left(\frac{2\tau_m}{\tau_0}\right) + 2\left[x - xh_{\text{dip}} + \ln\left(-\frac{\tau_m}{\tau_0 \ln\epsilon}\right)\right]\right\}}\right], \quad (6)$$

where ϵ is the tolerance assigned to the change in ξ and $h_{\text{dip}} = 0$ for the noninteracting case or $h_{\text{dip}} = h_{\text{dip border}}(x \gg 1)$ for the interacting case (see Sec. III B). If we look at Eq. (6) in more detail, we recognize the limit of "large" MNPs ($x \gg 1$) that we already discuss throughout this paper. By taking the limit of $x \gg 1$ we obtain that $h_K^{\text{opt}} \rightarrow (1 - h_{\text{dip}})$, which explains why h_K^{opt} saturates to 1 in Fig. 5(a) and why it can assume values lower than 1 for the interacting cases (see Figs. 6 and 8).

This analytical formula, with a tolerance of $\epsilon = 1 \times 10^{-6}$ is also displayed in Fig. 9 (in dashed black lines). We can see that there is a good agreement between the analytical h_K^{opt} formula, the interface position, and the simulation data for MNPs with $\Phi = 30, 60$ nm. It is also notable that the correct frequency dependence of h_K^{opt} is achieved. However, for MNPs with $\Phi = 5$ nm, neither the interface nor the analytical h_K^{opt} formula are in agreement with the simulation results. The analytical approximation underestimates the value of h_K^{opt} due to the interface being broad, which is incompatible with the small decrease in the probability $\xi = 1 - \epsilon$ that we propose.

It would be very useful to determine in which cases thermal fluctuations affect the magnetic relaxation to assess the validity range of Eq. (6). Moreover, this will shed light on what is a "large" (i.e., not affected by thermal fluctuations) or "small" MNP (i.e., greatly affected by thermal fluctuations). For this purpose, we take the curves h_K^{opt} versus x in Figs. 5(a) and 8(a) and defined with all

these curves a maximum critical x value, x_C, to account for the "saturating" regime by allowing a detachment of this behavior approximately equal to 1% of the full h_K^{opt} range. We obtain $x_C = 9.1$ that is of the order of 10 as we predict in Sec. III A 3. This critical value is valid for MNPs with $M_S \sim 3.5 \times 10^5$ A m^{-1} and MFH frequencies, 100 kHz $\leq f \leq$ 1 MHz. For each particle we define its limit temperature:

$$T_{\text{no fluc}}(x) = \frac{x}{10}T_{\text{exp}}, \quad (7)$$

which divides the regime in which fluctuations do not affect the relaxation of a MNP ($T_{\text{exp}} < T_{\text{no fluc}}$) and the regime in which they do ($T_{\text{exp}} \geq T_{\text{no fluc}}$).

To illustrate the use of this definition, we present the $T_{\text{no fluc}}$ values associated with different x values (i.e., different MNP sizes) and the extreme MFH frequency conditions in Fig. 10. By analyzing it, we can conclude that both the $\Phi = 30$ nm and 60 nm MNPs are not significantly affected by thermal fluctuations and are what we call "large" MNPs in these experimental conditions, as their $T_{\text{no fluc}}$ values are above the temperature set in simulations ($T_{\text{exp}} = 300$ K). Consequently, the analytical approach (both the probability map and the close-form expression for h_K^{opt}) can be successfully applied in these cases to describe the magnetic behavior and to predict optimal conditions for MFH experiments. However, for MNPs with $\Phi = 5$ nm, the corresponding limit temperature is
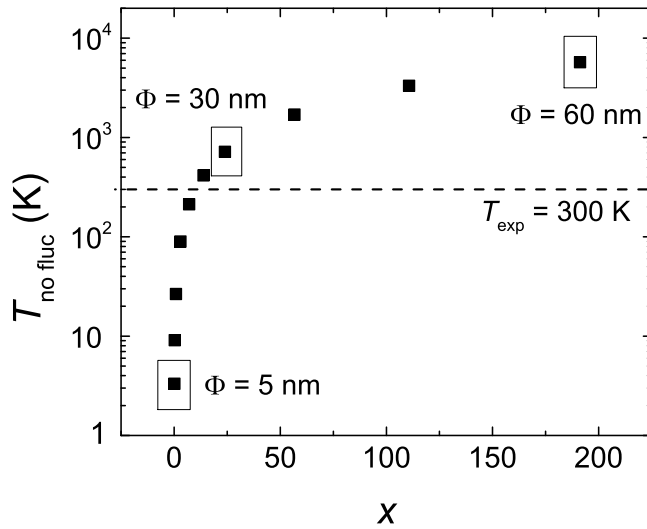
FIG. 10.   Limit temperature $T_{\text{no fluc}}$ as a function of $x = \mu_0 M_S V H_0/(k_B T)$. The temperature in which the simulated MFH experiments are made is represented with a dashed black line.

below the one used for the simulations, which means that the analytical formulas do not describe the behavior of the system and cannot be applied.

In conclusion, this analytical approach can guide us for synthesizing MNPs with an enhanced SPA for MFH applications, providing information on the h_K^{opt} without a complete description of the hysteresis loops. Moreover, we give a simple thermal interpretation of the validity range of our analytical predictions.

D. Randomly oriented MNPs and chains

In the previous sections, we analyze MNP systems with easy axes parallel to the external ac field but sometimes it is impossible to align the MNPs or chains experimentally. We analyze how area curves change for randomly oriented MNPs or randomly oriented chains with respect to the case of MNPs with easy axes oriented parallel to the external field.

We use the azimuthal symmetry of the problem, discretizing the values of the polar orientation angle ϕ_n, and weight the value of the corresponding area by the solid angle ($\sin\phi_n$), avoiding unnecessary sweeps of the azimuthal angle. In this particular case, we take 91 MNPs or chains with consecutive, equally spaced orientations $0 < \phi_n < \pi/2$. In Fig. 11, we present the area curves for these randomly oriented systems and the parallelly oriented analogs for comparison.

For the noninteracting cases, we compare MNPs with randomly oriented anisotropy axes with MNPs whose anisotropy axes are oriented parallel to the external field. It is worth noting that experimentally, in most cases, the configuration for noninteracting systems is that of randomly oriented anisotropy axes. Therefore, even if it is not the
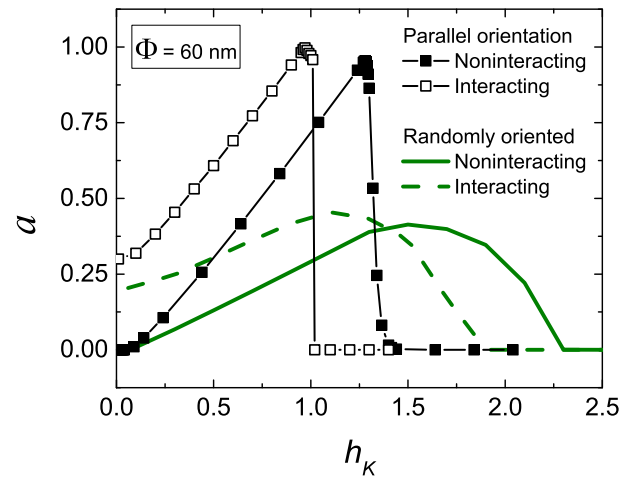

FIG. 11.   Comparison between the curves of normalized hysteresis area a as a function of the relative anisotropy field h_K for parallelly and randomly oriented noninteracting MNPs and interacting chains of MNPs for experimental frequency $f = 100$ kHz and diameter $\Phi = 60$ nm. The ratio between the diameter and interparticle spacing is fixed in $\Phi/d = 0.5$ for the interacting cases. Here "orientation" refers to the direction of the MNPs' easy axes.

most favorable case, having random orientations in MNP systems is something usual that needs to be analyzed.

When comparing the randomly oriented systems, we notice that the effect of interactions is the same as we have already analyzed during our work: interactions shift the curve towards lower h_K values. Moreover, if we look at regions I and II, we realize that the hysteresis area obtained for parallelly oriented chains is always equal or greater than the area for randomly oriented chains. This highlights the relevance of controlling the orientation of MNP structures in a MFH experiment, since it can increase the SPA considerably. Having control over the orientation of the linear arrangements gives us the possibility of placing the chains in the direction of the external magnetic field, which is the most favorable in terms of SPA [47].

The main difference between parallel and random orientations, apart from the magnitude of the enclosed area, is that for randomly oriented axes or chains, the regions expand to a wider h_K range, which provides the opportunity of having a similar behavior for various H_K in the same experimental setup (fixed H_0) and the setback of having to use a broader range of H_0 to allow a sample with a given H_K to switch regions.

IV. CONCLUSIONS

We simulate MNP systems exposed to an ac field and address the effect of both particle-intrinsic parameters (such as particle size and anisotropy) and experimental conditions (frequency) for MFH applications. The effects

are evaluated through the area A enclosed by the hysteresis loop of the system, as the SPA $\sim A$.

Both the noninteracting and interacting (linear chain) MNP systems show the presence of four regions of different behavior in the area as a function of the relative anisotropy curve ("area curve"). Two of these regions correspond to major loops (regions I and II) and the other two to minor loops (regions III and IV). Regardless of frequency and interactions, a maximum is always reached for the enclosed loop area (which is associated with the transition from region II to region III). While the area curves as a function of relative anisotropy are qualitatively similar, the relative anisotropy range and the limits between regions are modified by size Φ, frequency f, and interactions.

During our analysis, we realize that thermal fluctuations play a key role in the predictability of our system's behavior and that a parameter that reflects the influence of fluctuations is $x = \mu_0 M_S V H_0/(k_B T)$. The larger MNPs analyzed provided a limit in which fluctuations do not affect the relaxation significantly ($x \gg 1$). We explain differences in the area curves when changing Φ and f with the effect of thermal fluctuations on the magnetic moments, that "smooth" and "round" area curves and loops when $x \ll 1$. The area curves are powerful tools for the optimal design of MNPs with improved heating efficiency for MFH experiments through the selection of both intrinsic MNP parameters and experimental conditions (H_0, f).

For the interacting case, these changes have prominent consequences. We see that in low-relative-anisotropy cases, interactions help to increase the area of the hysteresis loops with respect to the noninteracting dispersed system, while in high-relative-anisotropy cases they are detrimental to the enclosed area. This fact, observed for a simple linear chain of MNPs, explains the diversity of apparently contradictory results concerning the influence of interactions on the SPA. The outcome of an experiment depends on the determination of the relative anisotropy condition (low or high) and on the characteristics of MNPs (K, x), as well as the frequency f and the initial working temperature T_{exp}. The problem can be posed as a comparison of the effective coercive field $H_C^{eff}(T_{exp}, K, x, f)$ with the applied ac field amplitude H_0. By increasing f, we see that thermal effects decrease, and as small MNPs are more affected by thermal fluctuations than large ones, the variation of f has a greater repercussion on their behavior. For the same reason, interactions affect large particles to a greater extent than small ones, even when assuming similar values of a local dipolar field acting on the MNPs of different sizes.

We find that the optimal condition (i.e., reaching the maximum SPA) is when thermal fluctuation effects on the relaxation of MNPs can be neglected (large x values, what we call "large" MNPs). In this case, the hysteresis loops are almost rectangular in shape and the systems cannot be described by the LRT, thus, other approaches are

needed to predict their behavior correctly. By tuning H_0 and $H_C^{eff}(T) \approx H_K^{eff}$, the desired maximum can be obtained. We define a limit temperature, $T_{no\ fluc}$, that allows us to identify if we are in the regime of no thermal fluctuation influence ($T_{exp} \ll T_{no\ fluc}$), and for this case, we provide a closed-form expression for the optimal relative anisotropy value, h_K^{opt}.

Regarding random MNPs and chains, their area curves expand to a broader h_K range than the oriented easy axes case, but their optimal performance is worse than that of oriented MNPs and chains. However, when orientation is not possible, knowing the corresponding h_K^{opt} is vital to achieve the best performance from the randomly oriented system.

ACKNOWLEDGMENTS

APPENDIX A: MINOR LOOPS IN REGION III

We note during our analysis that a considerable decrease in the enclosed hysteresis area is given when going from region II to region III. We associate this behavior with a reduction in the fraction of MNPs fluctuating from one minimum to the other. A fact worth investigating is why interactions cause these minor loops to be off centered, as shown in Fig. 7(c).

Anisotropy is sufficiently high with respect to H_0; thus, not all magnetic moments can be inverted. This causes the loop to need several cyclings to reach dynamic equilibrium [55]. To understand this phenomena, we show in Fig. 12 the whole convergence-to-equilibrium process for the loops in Figs. 2(c) and 7(c).

Starting with the noninteracting case, the initial conditions are that each MNP (denoted by j) in the chain has the same probability to be in each minimum; so, initial minima populations are $P_0^j(0) = P_1^j(0) = 0.5$ for all j. The fraction of MNPs that can fluctuate in minimum 0 is proportional to the probability of being in the superparamagnetic regime L, the population of that minima $P_0(t)$ and the difference of the actual population with the equilibrium one, $P_0(t) - P_0^\infty$. We start sweeping at $h > 0$ for the virgin curve (from 0 to H_0). This breaks the symmetry of the problem by favoring minimum 0, which corresponds to the direction of the external field. The population of minimum
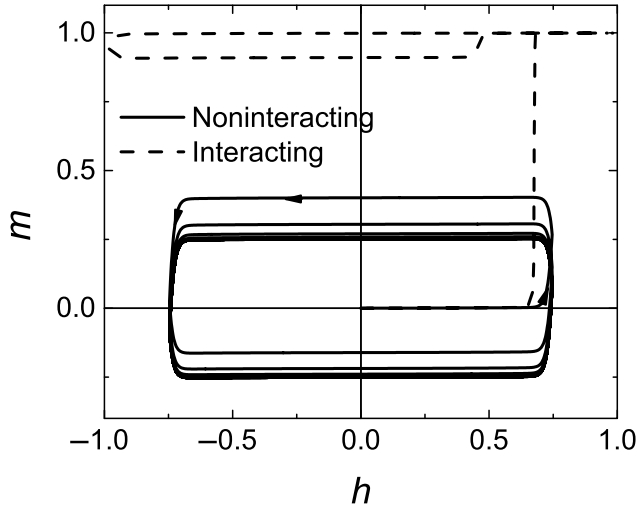
FIG. 12. Normalized magnetization hysteresis loops for MNPs with diameter $\phi = 60$ nm in region III for a noninteracting case ($h_K = 1.34$) and an interacting case ($h_K = 1.017$) for $\phi_n = 0$.

0 increases, as does m initially. We have an initial imbalance that is compensated for with each cycling, since they are symmetrical in terms of P_0 and P_1.

When adding interactions into the picture, the initial imbalance is indeed greater for this case: the field on each particle is now $h + h_{dip}$ and as $h_{dip} \sim m > 0$, minimum 0 is even more favored and generates an initial "accumulation" of magnetic moments that cannot be reverted. This is seen in Fig. 12; if we consider that the virgin curve for the interacting case reaches $m = 1$, whereas for the noninteracting case it does not. Moreover, the cycling is no longer symmetrical in terms of P_0 and P_1 because when h starts to diminish, the field on each MNP is still positive due to h_{dip}. In conclusion, interactions anchor magnetic moments in minimum 0, avoiding their fluctuation.

This distinctive behavior of magnetization reaching dynamic equilibrium is manifested not only in the shape and centering of the hysteresis loop, as outlined in Fig. 12, but also in a reduction of its enclosed area. This is the reason why, when considering interactions, the decrease in the area curve from region II into region III is more abrupt than that in the noninteracting case.

APPENDIX B: ESTIMATION OF THE EFFECTIVE ENERGY BARRIER

Our approximate expression of the energy barrier that separates the metastable from the absolute minimum is based on the consideration of the effective field on the particle.

For generality, we present the development of the expression for the interacting case. As we explain in Sec. III B, the inversion of the MNPs at the border of the

chain generates a "cascade" effect that leads to the inversion of the magnetic moments of the rest of the MNPs in the chain. Thus, when interaction strengths are moderate and interactions do not dominate over the energy barrier, the effective coercive field of the chain is very close to the effective coercive field of the border particles. Without loss of generality, we can evaluate the case of the border MNP to get the behavior of the chain. Our development is valid for MNPs with $x \gg 1$.

First, we examine the case of $T \to 0$ to latter incorporate the effect of thermal fluctuations to the development. Considering the energy of a MNP, given by Eq. (1), the effective field $\mathbf{H}_{eff}$ on a MNP is given by [67]

$$\mathbf{H}_{eff} = -\frac{1}{\mu_0}\nabla_\mu E = \mathbf{H} + \mathbf{H}_{dip} + \frac{2KV}{\mu_0\mu^2}(\hat{\mathbf{n}} \cdot \boldsymbol{\mu})\hat{\mathbf{n}}. \quad (B1)$$

We are interested in the inversion of the border MNP's magnetization on the ascending branch of the hysteresis loop, at an external field $\mathbf{H} = H_0\hat{\mathbf{x}}$. Let us consider the easy magnetization axis in the same direction, $\hat{\mathbf{n}} = \hat{\mathbf{x}}$. In Eq. (B1), the effective field is given by two contributions: the local field $\mathbf{H}_{loc} = \mathbf{H}_0 + \mathbf{H}_{dip}$ and the anisotropy field $\mathbf{H}_K = (2KV/\mu_0\mu^2)(\hat{\mathbf{n}} \cdot \boldsymbol{\mu})\hat{\mathbf{n}}$, that depends on the orientation of the magnetic moment. We focus on describing the behavior as a function of the anisotropy energy density when $\mathbf{H}_{loc}$ is fixed to explain the probability of inversion at the external field $H = H_0$, ξ (see Sec. III C).

Before the inversion (b.i.), magnetization of the MNP at the border is $\boldsymbol{\mu} = -\mu\hat{\mathbf{x}}$ and, as we discuss, the dipolar field on it is $\mathbf{H}_{dip} = -H_{dip\ border}\hat{\mathbf{x}}$. By evaluating Eq. (B1) before the inversion, we obtain $\mathbf{H}_{eff}(\text{b.i.}) = (H_0 - H_{dip\ border} - H_K)\hat{\mathbf{x}}$.

At $T \to 0$, while the anisotropy field surpasses the local field, the particle cannot invert its magnetic moment. The magnetic moment will be inverted (i.) when $H_{loc} = H_K$, which gives $E(\text{i.}) = 0$. The energy barrier is then

$$\Delta E = E(\text{i.}) - E(\text{b.i.}) = \mu_0\mu(H_K + H_{dip\ border} - H_0), \quad (B2)$$

and, in this limit case, the probability ξ will simply be $\xi = \theta(H_K - H_{loc})$, where $\theta(x)$ is the Heaviside step function.

An analogous development can be done for finite temperature. Inversion will again be given by the condition $E(\text{i.}) = 0$. The difference is that now all fields and values need to be corrected for the effect of thermal fluctuations. We denote corrected values with the symbol $\tilde{\ }$. The temperature-corrected version of Eq. (B2) is then $\Delta E = \mu_0\tilde{\mu}(\tilde{H}_K + \tilde{H}_{dip\ border} - H_0) = \mu_0\tilde{\mu}(\tilde{H}_C^{eff} - H_0)$, where we consider that the coercive field is modified by interactions to be consistent with our previous notation.

Our analytical approach is suitable to describe MNPs in the limit of $x \gg 1$ (which implies a rectangular-shaped

loop). Under this hypothesis, $\widetilde{\mu} = M_S V$ and $\widetilde{H}_C^{\text{eff}} = \widetilde{H}_K + \widetilde{H}_{\text{dip border}}$ can be corrected with Eq. (5), with $\widetilde{H}_{\text{dip border}}$ derived from Eq. (4) (multiplying by H_0). Finally, the energy barrier can be approximated by

$$\Delta E = M_S V[H_C^{\text{eff}}(T) - H_0]. \qquad \text{(B3)}$$

[1] K. McNamara and S. A. M. Tofail, Nanoparticles in biomedical applications, Adv. Phys. X **2,** 54 (2017).

[2] S. He, H. Zhang, Y. Liu, F. Sun, X. Yu, X. Li, L. Zhang, L. Wang, K. Mao, G. Wang, Y. Lin, Z. Han, R. Sabirianov, and H. Zeng, Maximizing specific loss power for magnetic hyperthermia by hard-soft mixed ferrites, Small **14,** 1800135 (2018).

[3] M. Boskovic, G. F. Goya, S. Vranjes-Djuric, N. Jovic, B. Jancar, and B. Antic, Influence of size distribution and field amplitude on specific loss power, J. Appl. Phys. **117,** 103903 (2015).

[4] M. Ma, Y. Wu, J. Zhou, Y. Sun, Y. Zhang, and N. Gu, Size dependence of specific power absorption of Fe_3O_4 particles in AC magnetic field, J. Magn. Magn. Mater. **268,** 33 (2004).

[5] H. Ghayour, M. Abdellahi, M. G. Nejad, A. Khandan, and S. Saber-Samandari, Study of the effect of the Zn^{2+} content on the anisotropy and specific absorption rate of the cobalt ferrite: The application of $Co_{1-x}Zn_xFe_2O_4$ ferrite for magnetic hyperthermia, J. Aust. Ceram. Soc. **54,** 223 (2018).

[6] A. ur Rashid and S. Manzoor, Optimizing magnetic anisotropy of $La_{1-x}Sr_xMnO_3$ nanoparticles for hyperthermia applications, J. Magn. Magn. Mater. **420,** 232 (2016).

[7] P. Guardia, B. Batlle-Brugal, A. G. Roca, O. Iglesias, M. P. Morales, C. J. Serna, A. Labarta, and X. Batlle, Surfactant effects in magnetite nanoparticles of controlled size, J. Magn. Magn. Mater. **316,** e756 (2007).

[8] A. G. Roca, R. Costo, A. F. Rebolledo, S. Veintemillas-Verdaguer, P. Tartaj, T. González-Carreño, M. P. Morales, and C. J. Serna, Progress in the preparation of magnetic nanoparticles for applications in biomedicine, J. Phys. D **42,** 224002 (2009).

[9] A. P. Khandhar, R. M. Ferguson, J. A. Simon, and K. M. Krishnan, Tailored magnetic nanoparticles for optimizing magnetic fluid hyperthermia, J. Biomed. Mater. Res. Part A **100A,** 728 (2012).

[10] K. Kekalo, I. Baker, R. Meyers, and J. Shyong, Magnetic nanoparticles with high specific absorption rate at low alternating magnetic field, Nano Life **5,** 1550002 (2015).

[11] T. E. Torres, E. Lima, Jr., M. P. Calatayud, B. Sanz, A. Ibarra, R. Fernández-Pacheco, A. Mayoral, C. Marquina, M. R. Ibarra, and G. F. Goya, The relevance of Brownian relaxation as power absorption mechanism in magnetic hyperthermia, Sci. Rep. **9,** 3992 (2019).

[12] Y. Yuan and D.-A. Borca-Tasciuc, Comparison between experimental and predicted specific absorption rate of functionalized iron oxide nanoparticle suspensions, J. Magn. Magn. Mater. **323,** 2463 (2011).

[13] J. Carrey, B. Mehdaoui, and M. Respaud, Simple models for dynamic hysteresis loop calculations of magnetic single-domain nanoparticles: Application to magnetic hyperthermia optimization, J. Appl. Phys. **109,** 083921 (2011).

[14] R. P. Tan, J. Carrey, and M. Respaud, Magnetic hyperthermia properties of nanoparticles inside lysosomes using kinetic Monte Carlo simulations: Influence of key parameters and dipolar interactions, and evidence for strong spatial variation of heating power, Phys. Rev. B **90,** 214421 (2014).

[15] E. A. Périgo, G. Hemery, O. Sandre, D. Ortega, E. Garaio, F. Plazaola, and F. J. Teran, Fundamentals and advances in magnetic hyperthermia, Appl. Phys. Rev. **2,** 041302 (2015).

[16] G. T. Landi, Role of dipolar interaction in magnetic hyperthermia, Phys. Rev. B **89,** 014403 (2014).

[17] R. Fu, Y. Yan, C. Roberts, Z. Liu, and Y. Chen, The role of dipole interactions in hyperthermia heating colloidal clusters of densely-packed superparamagnetic nanoparticles, Sci. Rep. **8,** 4704 (2018).

[18] C. Martínez-Boubeta, K. Simeonidis, A. Makridis, M. Angelakeris, O. Iglesias, P. Guardia, A. Cabot, L. Yedra, S. Estradé, F. Peiró, Z. Saghi, P. Midgley, I. Conde-Leborán, D. Serantes, and D. Baldomir, Learning from nature to improve the heat generation of iron-oxide nanoparticles for magnetic hyperthermia applications, Sci. Rep. **3,** 1652 (2013).

[19] E. Lima, Jr., E. De Biasi, M. Vasquez Mansilla, M. E. Saleta, M. Granada, H. E. Troiani, F. B. Effenberger, L. M. Rossi, H. R. Rechenberg, and R. D. Zysler, Heat generation in agglomerated ferrite nanoparticles in an alternating magnetic field, J. Phys. D **46,** 045002 (2012).

[20] B. Sanz, R. Cabreira-Gomes, T. E. Torres, D. P. Valdés, E. Lima, Jr., E. De Biasi, R. D. Zysler, M. R. Ibarra, and G. F. Goya, Low-dimensional assemblies of magnetic $MnFe_2O_4$ nanoparticles and direct in vitro measurements of enhanced heating driven by dipolar interactions: Implications for magnetic hyperthermia, ACS Appl. Nano Mater. **3,** 8719 (2020).

[21] M. K. Kuimova, G. Yahioglu, J. A. Levitt, and K. Suhling, Molecular rotor measures viscosity of live cells via fluorescence lifetime imaging, J. Am. Chem. Soc. **130,** 6672 (2008).

[22] M. K. Kuimova, S. W. Botchway, A. W. Parker, M. Balaz, H. A. Collins, H. L. Anderson, K. Suhling, and P. R. Ogilby, Imaging intracellular viscosity of a single cell during photoinduced cell death, Nat. Chem. **1,** 69 (2009).

[23] B. Sanz, M. P. Calatayud, E. De Biasi, E. Lima, Jr., M. Vasquez Mansilla, R. D. Zysler, M. R. Ibarra, and G. F. Goya, *In silico* before *in vivo*: How to predict the heating efficiency of magnetic nanoparticles within the intracellular space, Sci. Rep. **6,** 38733 (2016).

[24] M. Jeun, Y. J. Kim, K. H. Park, S. H. Paek, and S. Bae, Physical contribution of Néel and Brown relaxation to interpreting intracellular hyperthermia characteristics using superparamagnetic nanofluids, J. Nanosci. Nanotechnol. **13,** 5719 (2013).

[25] J.-P. Fortin, F. Gazeau, and C. Wilhelm, Intracellular heating of living cells through Néel relaxation of magnetic nanoparticles, Eur. Biophys. J. **37,** 223 (2007).

[26] M. Anand, Thermal and dipolar interaction effect on the relaxation in a linear chain of magnetic nanoparticles, J. Magn. Magn. Mater. **522,** 167538 (2021).

[27] M. Anand, V. Banerjee, and J. Carrey, Relaxation in one-dimensional chains of interacting magnetic nanoparticles: Analytical formula and kinetic Monte Carlo simulations, Phys. Rev. B **99,** 024402 (2019).

[28] N. A. Usov and Y. B. Grebenshchikov, Hysteresis loops of an assembly of superparamagnetic nanoparticles with uniaxial anisotropy, J. Appl. Phys. **106,** 023917 (2009).

[29] I. Rodrigo, I. Castellanos-Rubio, E. Garaio, O. K. Arriortua, M. Insausti, I. Orue, J. Á. García, and F. Plazaola, Exploring the potential of the dynamic hysteresis loops via high field, high frequency and temperature adjustable AC magnetometer for magnetic hyperthermia characterization, Int. J. Hyperther. **37,** 976 (2020).

[30] M. Anand, Hysteresis in a linear chain of magnetic nanoparticles, J. Appl. Phys. **128,** 023903 (2020).

[31] M. Anand, J. Carrey, and V. Banerjee, Spin morphologies and heat dissipation in spherical assemblies of magnetic nanoparticles, Phys. Rev. B **94,** 094425 (2016).

[32] M. Palihawadana-Arachchige, H. Nemala, V. M. Naik, and R. Naik, Effect of magnetic dipolar interactions on temperature dependent magnetic hyperthermia in ferrofluids, J. Appl. Phys. **121,** 023901 (2017).

[33] F. H. Sánchez, P. Mendoza Zélis, M. L. Arciniegas, G. A. Pasquevich, and M. B. Fernández van Raap, Dipolar interaction and demagnetizing effects in magnetic nanoparticle dispersions: Introducing the mean-field interacting superparamagnet model, Phys. Rev. B **95,** 134421 (2017).

[34] O. Laslett, S. Ruta, J. Barker, R. W. Chantrell, G. Friedman, and O. Hovorka, Interaction effects enhancing magnetic particle detection based on magneto-relaxometry, Appl. Phys. Lett. **106,** 012407 (2015).

[35] D. F. Coral, P. Mendoza Zélis, M. Marciello, M. del P. Morales, A. Craievich, F. H. Sánchez, and M. B. Fernández van Raap, Effect of nanoclustering and dipolar interactions in heat generation for magnetic hyperthermia, Langmuir **32,** 1201 (2016).

[36] P. Hugounenq, M. Levy, D. Alloyeau, L. Lartigue, E. Dubois, V. Cabuil, C. Ricolleau, S. Roux, C. Wilhelm, F. Gazeau, and R. Bazzi, Iron oxide monocrystalline nanoflowers for highly efficient magnetic hyperthermia, J. Phys. Chem. C **116,** 15702 (2012).

[37] S. Behrens, W. Habicht, K. Wagner, and E. Unger, Assembly of nanoparticle ring structures based on protein templates, Adv. Mater. **18,** 284 (2006).

[38] E. Myrovali, N. Maniotis, A. Makridis, A. Terzopoulou, V. Ntomprougkidis, K. Simeonidis, D. Sakellari, O. Kalogirou, T. Samaras, R. Salikhov, M. Spasova, M. Farle, U. Wiedwald, and M. Angelakeris, Arrangement at the nanoscale: Effect on magnetic particle hyperthermia, Sci. Rep. **6,** 37934 (2016).

[39] I. Morales, R. Costo, N. Mille, G. B. Da Silva, J. Carrey, A. Hernando, and P. De la Presa, High frequency hysteresis losses on γ-Fe$_2$O$_3$ and Fe$_3$O$_4$: Susceptibility as a magnetic stamp for chain formation, Nanomaterials **8,** 970 (2018).

[40] I. Orue, L. Marcano, P. Bender, A. García-Prieto, S. Valencia, M. A. Mawass, D. Gil-Cartón, D. Alba Venero, D. Honecker, A. García-Arribas, L. Fernández Barquín, A. Muela, and M. L. Fdez-Gubieda, Configuration of the magnetosome chain: A natural magnetic nanoarchitecture, Nanoscale **10,** 7407 (2018).

[41] D. Serantes, K. Simeonidis, M. Angelakeris, O. Chubykalo-Fesenko, M. Marciello, M. del P. Morales, D. Baldomir, and C. Martínez-Boubeta, Multiplying magnetic hyperthermia response by nanoparticle assembling, J. Phys. Chem. C **118,** 5927 (2014).

[42] S. Ghaisari, M. Winklhofer, P. Strauch, S. Klumpp, and D. Faivre, Magnetosome organization in magnetotactic bacteria unraveled by ferromagnetic resonance spectroscopy, Biophys. J. **113,** 637 (2017).

[43] L. C. Branquinho, M. S. Carrião, A. S. Costa, N. Zufelato, M. H. Sousa, R. Miotto, R. Ivkov, and A. F. Bakuzis, Effect of magnetic dipolar interactions on nanoparticle heating efficiency: Implications for cancer hyperthermia, Sci. Rep. **3,** 2887 (2013).

[44] A. Y. Zubarev, Effect of internal chain-like structures on magnetic hyperthermia in non-liquid media, Phil. Trans. R. Soc. A **377,** 20180213 (2019).

[45] A. F. Abu-Bakr and A. Zubarev, Effect of interparticle interaction on magnetic hyperthermia: Homogeneous spatial distribution of the particles, Phil. Trans. R. Soc. A **377,** 20180216 (2019).

[46] B. Mehdaoui, R. P. Tan, A. Meffre, J. Carrey, S. Lachaize, B. Chaudret, and M. Respaud, Increase of magnetic hyperthermia efficiency due to dipolar interactions in low-anisotropy magnetic nanoparticles: Theoretical and experimental results, Phys. Rev. B **87,** 174419 (2013).

[47] D. P. Valdés, E. Lima, Jr., R. D. Zysler, and E. De Biasi, Modeling the Magnetic Hyperthermia Response of Linear Chains of Nanoparticles with low Anisotropy: A key to Improving Specific Power Absorption, Phys. Rev. Appl. **14,** 014023 (2020).

[48] L. M. Armijo, Y. I. Brandt, D. Mathew, S. Yadav, S. Maestas, A. C. Rivera, N. C. Cook, N. J. Withers, G. A. Smolyakov, N. L. Adolphi, T. C. Monson, D. L. Huber, H. D. Smyth, and M. Osiński, Iron oxide nanocrystals for magnetic hyperthermia applications, Nanomaterials **2,** 134 (2012).

[49] E. Garaio, J. M. Collantes, J. A. Garcia, F. Plazaola, S. Mornet, F. Couillaud, and O. Sandre, A wide-frequency range AC magnetometer to measure the specific absorption rate in nanoparticles for magnetic hyperthermia, J. Magn. Magn. Mater. **368,** 432 (2014).

[50] E. C. Stoner and E. P. Wohlfarth, A mechanism of magnetic hysteresis in heterogeneous alloys, Phil. Trans. R. Soc. A **240,** 599 (1948).

[51] E. De Biasi, R. D. Zysler, C. A. Ramos, and M. Knobel, A new model to describe the crossover from superparamagnetic to blocked magnetic nanoparticles, J. Magn. Magn. Mater. **320,** e312 (2008).

[52] J. A. De Toro, P. S. Normile, S. S. Lee, D. Salazar, J. L. Cheong, P. Muñiz, J. M. Riveiro, M. Hillenkamp, F. Tournus, A. Tamion, and P. Nordblad, Controlled close-packing of ferrimagnetic nanoparticles: An assessment of the role of interparticle superexchange versus dipolar interactions, J. Phys. Chem. C **117,** 10213 (2013).

[53] J. A. De Toro, S. S. Lee, D. Salazar, J. L. Cheong, P. S. Normile, P. Muñiz, J. M. Riveiro, M. Hillenkamp, F. Tournus, A. Tamion, and P. Nordblad, A nanoparticle replica of the spin-glass state, Appl. Phys. Lett. **102**, 183104 (2013).

[54] P. Nordblad, Competing interaction in magnets: The root of ordered disorder or only frustration? Phys. Scr. **88**, 058301 (2013).

[55] P. Allia, G. Barrera, and P. Tiberto, Hysteresis effects in magnetic nanoparticles: A simplified rate-equation approach, J. Magn. Magn. Mater. **496**, 165927 (2019).

[56] M. Coduri, P. Masala, L. Del Bianco, F. Spizzo, D. Ceresoli, C. Castellano, S. Cappelli, C. Oliva, S. Checchia, M. Allieta, D.-V. Szabo, S. Schlabach, M. Hagelstein, C. Ferrero, and M. Scavini, Local structure and magnetism of Fe_2O_3 maghemite nanocrystals: The role of crystal dimension, Nanomaterials **10**, 867 (2020).

[57] H. G. Parmar, I. S. Smolkova, N. E. Kazantseva, V. Babayan, M. Pastorek, and N. Pizurova, Heating efficiency of iron oxide nanoparticles in hyperthermia: Effect of preparation conditions, IEEE Trans. Magn. **50**, 5200504 (2014).

[58] I. Hilger, In vivo applications of magnetic nanoparticle hyperthermia, Int. J. Hyperther. **29**, 828 (2013).

[59] D. Bobo, K. J. Robinson, J. Islam, K. J. Thurecht, and S. R. Corrie, Nanoparticle-based medicines: A review of FDA-approved materials and clinical trials to date, Pharm. Res. **33**, 2373 (2016).

[60] L. Zhu, Z. Zhou, H. Mao, and L. Yang, Magnetic nanoparticles for precision oncology: Theranostic magnetic iron oxide nanoparticles for image-guided and targeted cancer therapy, Nanomedicine (Lond.) **12**, 73 (2017).

[61] A. C. Anselmo and S. Mitragotri, A review of clinical translation of inorganic nanoparticles, AAPS J. **17**, 1041 (2015).

[62] I. Conde-Leborán, D. Serantes, and D. Baldomir, Orientation of the magnetization easy axes of interacting nanoparticles: Influence on the hyperthermia properties, J. Magn. Magn. Mater. **380**, 321 (2015).

[63] R. E. Rosensweig, Heating magnetic fluid with alternating magnetic field, J. Magn. Magn. Mater. **252**, 370 (2002).

[64] S. Dutz and R. Hergt, Magnetic nanoparticle heating and heat transfer on a microscale: Basic principles, realities and physical limitations of hyperthermia for tumour therapy, Int. J. Hyperther. **29**, 790 (2013).

[65] W. J. Atkinson, I. A. Brezovich, and D. P. Chakraborty, Usable frequencies in hyperthermia with thermal seeds, IEEE Trans. Biomed. Eng. **31**, 70 (1984).

[66] E. De Biasi, J. Curiale, and R. D. Zysler, Quantitative study of FORC diagrams in thermally corrected Stoner–Wohlfarth nanoparticles systems, J. Magn. Magn. Mater. **419**, 580 (2016).

[67] J. Leliaert, M. Dvornik, J. Mulkers, J. De Clercq, M. V. Milošević, and B. Van Waeyenberge, Fast micromagnetic simulations on GPU – recent advances made with mumax, J. Phys. D: Appl. Phys. **51**, 123002 (2018).